



# Mathematical Modeling for Angiogenesis

Tatsuya Hayashi<sup>(✉)</sup>

Graduate School of Information Science and Technology, Hokkaido University,  
Sapporo, Japan  
[thayashi@ist.hokudai.ac.jp](mailto:thayashi@ist.hokudai.ac.jp)

**Abstract.** Angiogenesis is the morphogenetic phenomenon in which new blood vessels emerge from an existing vascular network and configure a new network. To understand complex movements of endothelial cells and molecular processes that drive angiogenic morphogenesis, time-lapse live imaging of dynamic collective cell migration and mathematical modeling have proven highly informative. This paper focuses on recent mathematical models for the dynamics of endothelial cells during angiogenesis and presents the importance of both repulsive and attractive two-body interactions by showing results of simulation.

## 1 Introduction

Angiogenesis is a phenomenon that new blood vessels are formed by sprouting from existing vessels. Branch elongation and bifurcation during angiogenesis are driven by collective motion of endothelial cells (ECs). Angiogenesis occurs in response to tissue ischemia or increased oxygen demand during various processes such as wound healing, placenta formation and tumor growth. Therefore, elucidation of mechanisms of angiogenesis is essential to expand our knowledge about physiological and pathological phenomena.

Collective cell migration in morphogenesis is often regulated by leader cells, which are accompanied by other follower cells that uniformly migrate. As for angiogenic elongation, an EC called a “tip cell”, is commonly thought to migrate in the direction of new vessel [1, 2]. The adjacent ECs are assumed to follow the tip cell as stalk cells connected to each other through cell-cell junctions. However, experiments with time-lapse live imaging have revealed that cell migration during angiogenic morphogenesis involves complex behavior. Individual ECs exhibit dynamic and heterogeneous motion, move forwards and backward along the path of the elongation and change often their positions even at the tips. This ‘cell mixing’ effect was observed in both *in vitro* and *in vivo* experiments [3, 4]. Furthermore, Sugihara *et al.* observed the dynamics of ECs in sprouting blood vessels of zebrafish and found that the movement of tip cells depends on the presence of stalk cells within a proper distance [5]. For a tip cell and stalk cells moving forward along the elongating branch, the isolated tip cell stopped moving after a laser shot ablated the follower EC. However, the tip cell started moving again when another EC approached it. This result suggests that the

interaction between ECs plays an essential role in the complex multicellular dynamics in angiogenesis. To uncover hidden laws driving angiogenic morphogenesis, Takubo *et al.* analyzed EC behaviors in an *in vitro* angiogenic sprouting assay using mouse aortic explants [6]. Time-lapse imaging of sprouting from cell sheets around tissue explants showed directional collective cell movements with frequent U-turns. Imaging of isolated branches with basal cell sheets removed revealed that a constant supply of migrating cells is required for ECs to branch forward.

A lot of mathematical models for angiogenesis have been proposed from various points of view: a hybrid model of cell migration on an elastic matrix of fibers [7], a mesoscopic lattice-based stochastic model in relation to deterministic continuous models [8], a phase-field continuous model of sprouting angiogenesis described by compact partial differential equations [9], and continuous model described by differential equations [10]. A stochastic states model and the differential equation model corresponding to its continuous limit have been discussed to explain the observation in the dynamics of ECs along an elongating branch [5]. Matsuya *et al.* focused on the effects of cell-to-cell interaction and proposed a one-dimensional discrete model that incorporates deterministic two-body interaction between ECs, which do not consider stochastic fluctuation and a gradient distribution of angiogenic factors such as vascular endothelial growth factor (VEGF) [11]. This model has succeeded in explaining complex EC behaviors by cell-to-cell interactions. Takubo *et al.* quantitatively verified the two-body interaction, which had not been quantified in the one-dimensional model. Furthermore, they extended the model to take into account the interaction, which is thought to be caused by the polarity of ECs.

In Sect. 2, we present the one-dimensional model proposed by Matsuya *et al.* and show numerical simulation results. A power-law scaling behavior in this model is shown and analyzed. We present the extended model and a parameter estimation in Sect. 3. Section 4 is devoted to concluding remarks.

## 2 Discrete Dynamics System Model for Angiogenesis

The system is essentially two dimensional because murine aortic rings were embedded and ECs were cultured in collagen gel placed in a shallow petri dish. We neglect the effects of anastomosis(reconstruction of vessels) and cell division of ECs in neogenetic vessels. Actually cell division is rarely observed in the time span of the experiment ( $\sim 5\%$  a day). We consider formation of one of the newly generated blood vessel networks which arise from the aortic ring. We suppose that there is no neogenetic vessel sprouts in a certain direction according to the supply of ECs for  $t > 0$ . The  $n$ th ( $n = 0, 1, 2, \dots$ ) EC comes to the origin of this neogenetic vessel network at time step  $t = \sum_{i=1}^n a_i$  with an initial velocity  $v_{ini}(n) \geq 0$ , where  $a_i \in \mathbb{Z}_+$  is the time interval between the incidence of  $i$ th EC and that of  $(i-1)$ th EC. Here, we focus on the dynamics of ECs only in the first neogenetic vessel and the effects of two-body interactions between ECs in a branch. Interactions among ECs are quite complicated and have not been well uncovered. We assume that the interaction between ECs is caused by direct contact

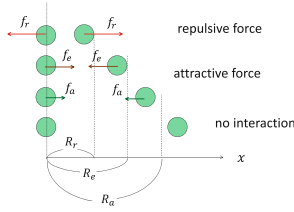


**Fig. 1.** Schematic figure of two-body interaction in the present model.

of their membranes; chemical signals or mechanical force induced by cell-to-cell contact yields the driving force of ECs. For short distance, the interaction force will turn out to be repulsive due to excluded volume effect, while it will turn out to be attractive if the distance becomes larger because of the interaction with pseudopodia. Thus the mathematical model we present here is given as

$$x_n^{t+1} - x_n^t = v_n^t \quad (1)$$

$$v_n^{t+1} - v_n^t = -\gamma v_n^t + \sum_{k \neq n} F(x_n^t - x_k^t), \quad (2)$$

where  $x_n^t \geq 0$  is the position of the  $n$ th EC at time step  $t \in \mathbb{Z}_+$ , the time unit ( $\Delta t = 1$ ) may correspond to the specific response time, the parameter  $\gamma$  ( $0 < \gamma < 1$ ) denotes the coefficient of conflict, and  $F$  denotes the two-body interaction between ECs.

The interaction  $F$  is adopted the following simple form by taking the three characteristic lengths  $R_r, R_e, R_a$  into account:

$$F(x) := \begin{cases} \operatorname{sgn}(x)f_r & (0 < |x| \leq R_r) \\ -\operatorname{sgn}(x)f_e & (R_r < |x| \leq R_e) \\ -\operatorname{sgn}(x)f_a & (R_e < |x| \leq R_a) \\ 0 & (R_a < |x|) \end{cases} \quad (3)$$

where  $\operatorname{sgn}(x) := x/|x|$  and  $f_r, f_e, f_a$  are the positive constant for interaction strengths (Fig. 1). Although the case  $x_n^t = x_k^t$  ( $n \neq k$ ) may be possible in principle, practically this model can neglect this case in numerical simulation.

Equation (1) means that  $v_n^t$  is the velocity of the  $n$ th EC at time step  $t$  and (2) is the discrete analogue of the Newtonian equation of motion. We do not consider the effect that ECs in the neogenetic vessels go back into the existing aortic ring, and  $x_n^t$  has to take non-negative value. To avoid back flow of ECs into the source, we reset  $x_n^{t+1} = 0$  and  $v_n^{t+1} = 0$  if  $x_n^{t+1} \leq 0$  in (1). In order to see

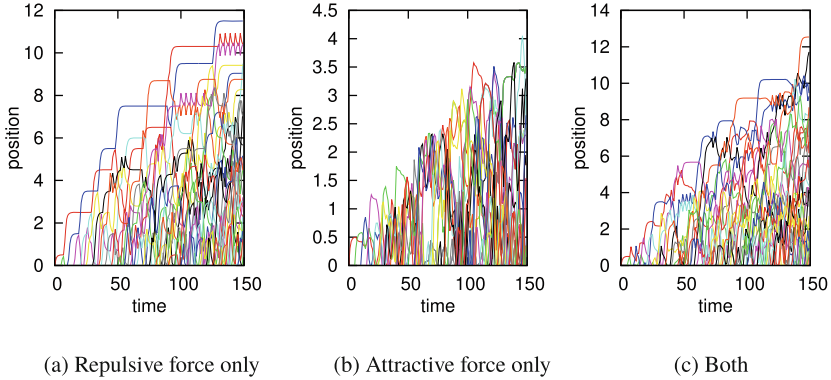


**Fig. 2.** Trajectories of EC movements during elongation with parameters  $R_r = 0.2$ ,  $R_e = 0.4$ ,  $R_a = 0.7$ ,  $\gamma = 0.6$ ,  $a = 5$ ,  $v_{ini} = 0.3$ ,  $v_{max} = 1.0$  and (a) Repulsive force only:  $f_r = 0.6$ ,  $f_e = 0$ ,  $f_a = 0$ , (b) Attractive force only:  $f_r = 0$ ,  $f_e = 0.15$ ,  $f_a = 0.05$  and (c) Both:  $f_r = 0.6$ ,  $f_e = 0.15$ ,  $f_a = 0.05$ .

the effects of repulsive and attractive interactions, we simulated (1) and (2) for three types of two-body interactions: (a) only repulsive ( $f_e \rightarrow -f_e$ ,  $f_a \rightarrow -f_a$  in (1)), (b) only attractive ( $f_r \rightarrow -f_r$ ), and (c) both interactions given in (1). A typical result is shown in Fig. 2, where we put  $a_i = a(\text{constant})$  and  $v_{ini}(i) = v_{ini}(\text{constant})$  for all  $i$ .

When interaction is only repulsive, the distribution of ECs is fairly uniform as shown in Fig. 2(a), while if interaction is only attractive, ECs clump together as in Fig. 2(b). In case both repulsive and attractive interactions coexist as is supposed in this model, ECs clearly show the cell mixing behavior and the distribution of ECs is sufficiently uniform. The cell mixing behavior is also seen in Fig. 2(a), though it is less frequent than in Fig. 2(c). As a consequence, repulsive interaction between ECs is necessary for smoothing the distribution of ECs and attractive interaction enhances the cell mixing behavior in the dynamics of ECs. Figure 4 shows the time dependence of the reaching position of ECs, that is, the position of an EC at the tip. As shown in Fig. 4(b), it almost scales as  $t^{2/3}$  for different strengths of attractive interaction. In fact, we can find that this exponent  $2/3$  is observed almost irrespective of the parameters for interactions, supply rate, and initial velocity. In particular, the data of numerical simulation closely fit, the curves  $\propto t^{2/3}$  in the case of no attractive interaction. For random walk, the reaching position scales as  $t^{1/2}$ , while it scales as  $t^1$  for wave propagation. The exponent  $2/3$  suggests that the ECs in the present model show the dynamics between random walk and wave propagation. The theoretical explanation of this universal exponent is given in Appendix.

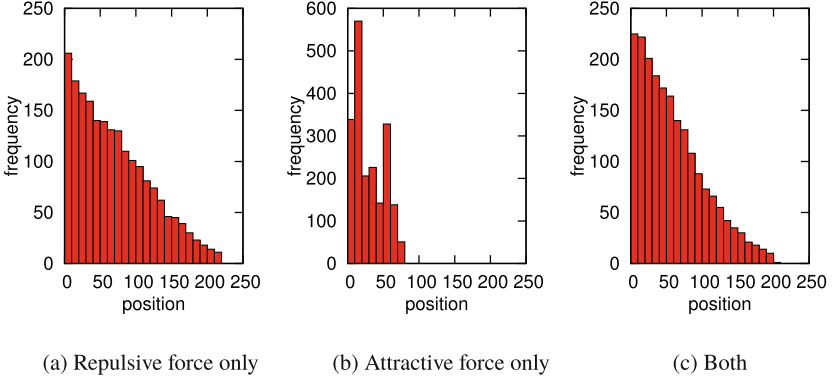


**Fig. 3.** Distributions of ECs at time step  $t = 10^4$ . Parameters are the same as those in Fig. 2.

### 3 A Two-Dimensional Model Considering the Anisotropic Nature of Two-Body Interactions

Under the assumption of simple two-body interactions between ECs, the mathematical model discussed in previous section successfully reproduced the cell mixing effects. However, the two-body interaction is not quantitatively validated. In this section, we present the parameter estimation of the model from the position data of ECs obtained by an automated cell tracking system. We first extended the one-dimensional model to a two-dimensional one as follows,

$$x_n^{t+1} - x_n^t = v_n^t \quad (4)$$

$$v_n^{t+1} - v_n^t = -\gamma v_n^t + \sum_{k \neq n} F(\|x_n^t - x_k^t\|) \frac{x_n^t - x_k^t}{\|x_n^t - x_k^t\|}, \quad (5)$$

where  $x_n^t \in \mathbb{R}^2$  and  $v_n^t \in \mathbb{R}^2$  are the position and the velocity of the  $n$ th EC at time step  $t$ , respectively, and  $\gamma > 0$  denotes the coefficient of damping. The interaction term is isotropic, which depends only on the relative positions  $x_n^t - x_k^t$  between two ECs. We estimate the parameter  $\gamma$  and the force function  $F$  from the experimental data of the time-lapse live imaging of ECs. The interaction between ECs are supposed to be short-range rather than long-range force. Therefore, let us consider the rectangular kernel on bounded support as the density kernel,

$$F(x) = \sum_{k=0}^{N-1} b_k \left( \theta \left( x - k \frac{R_d}{N} \right) - \theta \left( x - (k+1) \frac{R_d}{N} \right) \right), \quad (6)$$

Here  $R_d$  is the upper bound distance of cell-to-cell interaction, the range  $[0, R_d]$  is divided into  $N$  equal intervals, and  $\theta$  denotes the step function:

$$\theta(x) := \begin{cases} 1 & (x > 0) \\ 0 & (x \leq 0) \end{cases} \quad (7)$$

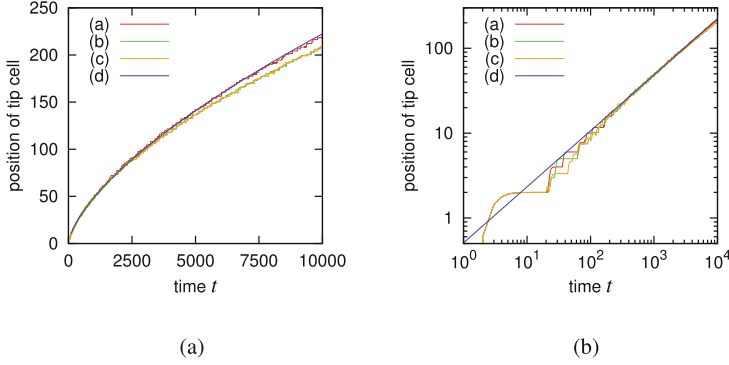


**Fig. 4.** (a) The parameters are  $R_r = 0.2$ ,  $R_e = 0.4$ ,  $R_a = 0.7$ ,  $f_r = 0.6$ ,  $f_a = 0$ ,  $v_{ini} = 0$ ,  $\gamma = 0.6$ ,  $v_{max} = 1.0$ ,  $\langle a \rangle = 5$ , and (red curve)  $f_e = 0$ , (green curve)  $f_e = 0.2$ , (orange curve)  $f_e = 0.4$ . The blue curve satisfies  $y = 0.5092t^{0.6601}$ . (b) Log-log plot of the four curves in (a). The straight line satisfies  $\ln(y) = 0.6601 \ln(t) - 0.6749$ , which is fitted to the red curve. “ $\langle a \rangle = 5$ ” means that the injection period is random with average period 5.

Given  $N$  and  $R_d$ , we minimize the following error function  $E$  for the estimation of the parameter  $\gamma$  and  $b_k$  ( $k = 0, 1, \dots, N-1$ ):

$$E = \sum_t \sum_n \left\| \left( \bar{v}_n^{t+1} - \bar{v}_n^t \right) - \left( -\gamma \bar{v}_n^t + \sum_{k \neq n} F \left( \|\bar{x}_n^t - \bar{x}_k^t\| \right) \frac{\bar{x}_n^t - \bar{x}_k^t}{\|\bar{x}_n^t - \bar{x}_k^t\|} \right) \right\|^2, \quad (8)$$

where  $\bar{x}_n^t$  is experimentally obtained cell position of  $n$ th EC at time  $t$ , and  $\bar{v}_n^t$  is the velocity as numerical difference. Since  $E$  is a quadratic polynomial of  $N+1$  variables  $\gamma$  and  $\{b_k\}_{k=0}^{N-1}$ , the minimum of  $E$  is unique.

Figure 5 shows the estimated function  $F$  and potential from  $F$  when  $N = 25$  and  $R_d = 50 \mu\text{m}$ . ECs experience distance-dependent interactions: with repulsive force in  $\sim 8 \mu\text{m}$  and attractive force in  $8 \sim 30 \mu\text{m}$ . Since each EC has its own volume, proximity of two cells may produce the repulsive force as a result of excluded volume effects. On the other hand, the attractive force may reflect contact-dependence acceleration.

Furthermore, since the shape of an EC is anisotropic, we consider anisotropy of cellular interactions. The presence of ECs moving backward produces different pattern of directionality as follows: (i) two ECs move into the opposite direction apart from each other, (ii) two ECs move into the opposite direction approaching each other, (iii) two ECs move in the same direction. Based on these classifications, we extended Eq. (4) to the following equation.

$$\begin{aligned} v_n^{t+1} - v_n^t = & -\gamma v_n^t + \sum_{k \neq n} F_1 \left( \|\bar{x}_n^t - \bar{x}_k^t\| \right) \frac{\bar{x}_n^t - \bar{x}_k^t}{\|\bar{x}_n^t - \bar{x}_k^t\|} \theta \left( (\bar{x}_n^t - \bar{x}_k^t) \cdot v_n^t \right) \theta \left( -(\bar{x}_n^t - \bar{x}_k^t) \cdot v_k^t \right) \\ & + \sum_{k \neq n} F_2 \left( \|\bar{x}_n^t - \bar{x}_k^t\| \right) \frac{\bar{x}_n^t - \bar{x}_k^t}{\|\bar{x}_n^t - \bar{x}_k^t\|} \theta \left( -(\bar{x}_n^t - \bar{x}_k^t) \cdot v_n^t \right) \theta \left( (\bar{x}_n^t - \bar{x}_k^t) \cdot v_k^t \right) \end{aligned}$$

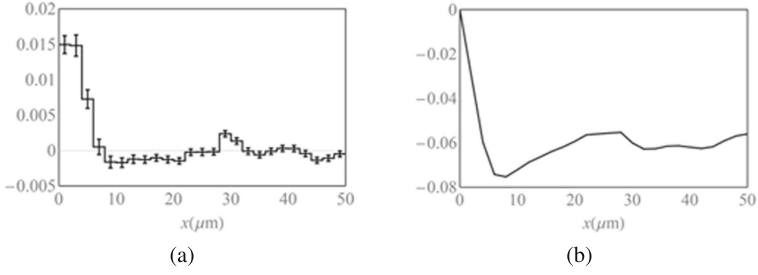


**Fig. 5.** (a) Estimated force  $F(x)$  with  $R_d = 50$ ,  $N = 25$ . (b)  $-\int_0^x F(\mu)d\mu$ , potential of (a).

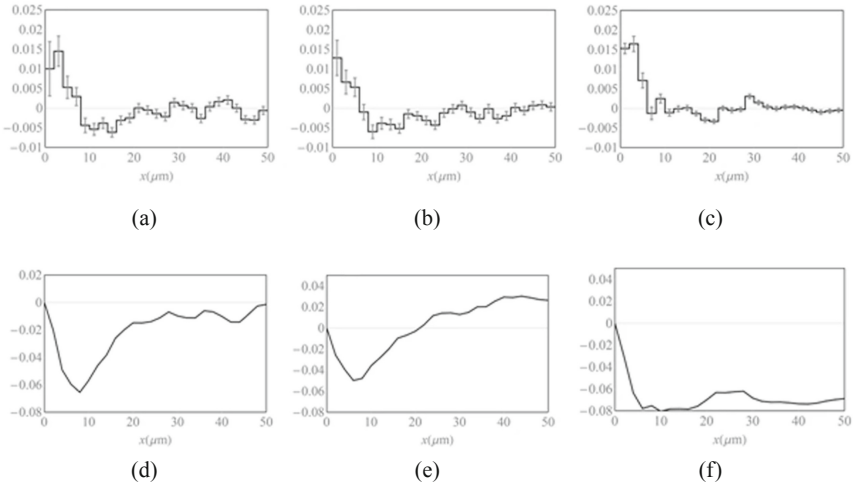


**Fig. 6.** Estimated force (a)  $F_1(x)$ , (b)  $F_2(x)$ , (c)  $F_3(x)$ . These functions were obtained in accordance with experimental results used in the estimation of  $F(x)$  (Fig. 5). Potentials of each forces, (d)  $-\int_0^x F_1(\mu)d\mu$ , (e)  $-\int_0^x F_2(\mu)d\mu$ , (f)  $-\int_0^x F_3(\mu)d\mu$ , respectively.

$$\begin{aligned}
 & + \sum_{k \neq n} F_3 (\|x_n^t - x_k^t\|) \frac{x_n^t - x_k^t}{\|x_n^t - x_k^t\|} \theta ((x_n^t - x_k^t) \cdot v_n^t) \theta ((x_n^t - x_k^t) \cdot v_k^t) \\
 & + \sum_{k \neq n} F_3 (\|x_n^t - x_k^t\|) \frac{x_n^t - x_k^t}{\|x_n^t - x_k^t\|} \theta (-(x_n^t - x_k^t) \cdot v_n^t) \theta (-(x_n^t - x_k^t) \cdot v_k^t)
 \end{aligned}$$

where the centered dot ‘ $\cdot$ ’ is the inner product and three force functions  $F_1$ ,  $F_2$ ,  $F_3$ , which correspond to the three patterns (i), (ii) and (iii), respectively, were estimated by a similar method as above. Figures 6(a)–(c) show the estimated three forces. In  $F_1$  and  $F_2$ , both repulsion ( $\sim 8 \mu\text{m}$ ) and attraction ( $8 \sim 30 \mu\text{m}$ ) were evident. By contrast,  $F_3$  contained only a repulsive component in  $\sim 8 \mu\text{m}$  with

no evident attractive component. Figures 6(d)–(f) are the integrals of Figs. 6(a)–(c) respectively, that is, potential. While Fig. 6(d) and (e) clearly indicate the positive slope (8~30  $\mu\text{m}$ ), Fig. 6(f) shows relatively flat in the region 6~50  $\mu\text{m}$ . Hence, it is suggested that an attractive interaction occurs between a pair of a cell moving forward and backward, resulting in accelerated cell movement when passing each other. On the contrary for lateral cells, attractive force is not much driven.

## 4 Concluding Remarks

In this paper, we have discussed a discrete dynamical model for angiogenesis which fits well some aspects of collective cell migration during angiogenesis. The dynamics of each ECs is assumed to be mainly ruled by deterministic two-body interactions which consist of short-range repulsion due to excluded volume effect and long-range force through pseudopodia and described by a one-dimensional discrete Newtonian equation of motion. Under this interaction, the tip position of a neogenetic vessel at time step  $t$ ,  $l(t)$ , develops as  $l(t) \propto t^{2/3}$ . We have given an interpretation on this value of exponent,  $2/3$ , based on the equation of continuity and a hypothesis of existence of a scaling function. Although this model has succeeded in explaining complex EC behaviors by cell-to-cell interactions based on simple Newtonian dynamics, the assumption of two-body interactions is not quantitatively validated. Furthermore, anisotropic nature of two-body interactions, which may be caused by cellular polarity, is not considered. The parameter estimation discussed in Sect. 3 revealed distance-dependent intercellular forces; a repulsive force in  $\sim 8 \mu\text{m}$  and attractive force in 8~20  $\mu\text{m}$ , which are consistent with the assumption of the one-dimensional model. These results suggest that the deterministic two-body interaction between ECs is an essential factor in complex EC behaviors such as cell mixing. However, these models deal with the early stage of angiogenesis and have not included chemotaxis, lumen formation, and remodeling of blood vessels, which are important in construction of *in vivo* blood vessel networks. Realistic mathematical modeling for angiogenesis and its application to medicine are an important issue. Development of the models by incorporating these factors is expected to uncover novel mechanisms and provide a theoretical framework for clinical trials targeting angiogenesis in the future.

**Acknowledgements.** The author would like to thank Prof. Tetsuji Tokihiro, Prof. Fumitaka Yura, Prof. Jun Mada, and Prof. Hiroki Kurihara for valuable comments.

## Appendix

Here, we explain the scaling law of the position of an EC at the tip according to the method in [11]. Let  $\rho(x, t)$  be the density of the ECs at time  $t$  and position  $x$ . In continuum limit,  $\rho(x, t)$  satisfies the equation of continuity:

$$\frac{\partial \rho(x, t)}{\partial t} + \frac{\partial}{\partial x} (\rho(x, t)v(x, t)) = 0, \quad (9)$$



where  $v(x, t)$  is the field of velocity ECs at  $(x, t)$ . From (1), in quasi equilibrium, we may approximate  $v(x, t)$  as

$$v(x, t) \sim \frac{1}{\gamma} \int F(x - y)\rho(y, t)dy. \quad (10)$$

If  $\rho(x, t)$  is a smooth function of  $x$ , we can expand

$$\rho(y, t) = \rho(x, t) + \frac{\partial \rho(x, t)}{\partial x}(y - x) + \frac{\partial^2 \rho(x, t)}{\partial x^2} \frac{(y - x)^2}{2} + \dots. \quad (11)$$

We further assume that higher derivatives of  $\rho(x, t)$  takes smaller absolute values than its first derivate  $\frac{\partial \rho(x, t)}{\partial x}$ . In fact, as shown in Figs. 3(a) and 3(c), the density  $\rho(x, t)$  is approximately a linear function, which implies that its higher order derivatives are negligible. Since  $F(x)$  is an odd function, neglecting the higher order terms, we have

$$v(x, t) \sim \frac{1}{\gamma} \int (y - x)F(x - y)\rho(y, t) \frac{\partial \rho(x, t)}{\partial x} dy =: A_{\text{eff}} \frac{\partial \rho(x, t)}{\partial x}, \quad (12)$$

where  $A_{\text{eff}}$  is a constant depending on the parameter  $\gamma, f_r, f_e, f_a, R_r, R_e, R_a$ . Hence, (9) gives

$$\frac{\partial \rho(x, t)}{\partial t} + A_{\text{eff}} \frac{\partial}{\partial x} \left( \rho(x, t) \frac{\partial \rho(x, t)}{\partial x} \right) = 0. \quad (13)$$

Suppose that  $\rho(x, t)$  has a scaling form with exponents  $\alpha, \beta$  as

$$\rho(x, t) = t^\alpha G\left(x/t^\beta\right). \quad (14)$$

Then, from (13), we have

$$t^{\alpha-1} \{\alpha G(X) - \beta X G'(X)\} + t^{2(\alpha-\beta)} A_{\text{eff}} \{G'(X)^2 + G(X)G''(X)\} \sim 0 \quad (X := x/t^\beta).$$

Hence, under the assumption of the scaling form (14), we find that

$$\alpha - 1 = 2(\alpha - \beta) \quad (15)$$

Since the number of ECs increases linearly in  $t$ ,

$$\int_0^{l(t)} \rho(x, t) dx = \frac{t}{\langle a \rangle}, \quad (16)$$

where  $l(t)$  is the position of the tip at which  $\rho(x, t) = 0$  and  $a$  is the average injection rate of ECs, and we have

$$t^{\alpha+\beta} \int_0^{X_l} G(X) dX = \frac{t}{\langle a \rangle}, \quad (17)$$

The constant  $X_l$  is considered to be the first 0 of  $G(X)$  for  $X > 0$  (or a cut-off length), and  $l(t) = X_l t^\beta$ . Since the integral of  $G(X)$  over  $X$  does not depend on time  $t$ , we have

$$\alpha + \beta = 1. \quad (18)$$

From (15) and (18), we obtain

$$\alpha = \frac{1}{3}, \beta = \frac{2}{3}. \quad (19)$$

Therefore,  $l(t) \propto t^{2/3}$  and the reaching position of ECs scales as  $t^{2/3}$ .

## References

1. Holderfield, M.T., Hughes, C.C.: Crosstalk between vascular endothelial growth factor, notch, and transforming growth factor-beta in vascular morphogenesis. *Circ. Res.* **102**, 637–652 (2008)
2. Smet, F.D., Segura, I., Bock, K.D., Hohensinner, P.J., Carmeliet, P.: Mechanisms of vessel branching: filopodia on endothelial tip cells lead the way. *Arterioscler. Thromb. Vasc. Biol.* **29**, 639–649 (2009)
3. Arima, S., et al.: Angiogenesis morphogenesis driven by dynamic and heterogeneous collective endothelial cell movement. *Development* **138**, 4763–4776 (2011)
4. Jakobsson, L., et al.: Endothelial cells dynamically compete for the tip cell position during angiogenic sprouting. *Nat. Cell Biol.* **12**, 943–953 (2010)
5. Sugihara, K., et al.: Autonomy and non-autonomy of angiogenic cell movements revealed by experiment-driven mathematical modeling. *Cell Rep.* **13**, 1814–1827 (2015)
6. Takubo, N., et al.: Cohesive and anisotropic vascular endothelial cell motility driving angiogenic morphogenesis. *Sci. Rep.* **9**, 9304 (2019)
7. Stéphanou, A., Floc’h, S.L., Chauvière, A.: A hybrid model to test the importance of mechanical cues driving cell migration in angiogenesis. *Math. Model. Nat. Phenom.* **10**, 142–165 (2015)
8. Spill, F., Guerrero, P., Alarcon, T., Maini, P.K., Byrne, H.M.: Mesoscopic and continuum modelling of angiogenesis. *J. Math. Biol.* **70**(3), 485–532 (2014). <https://doi.org/10.1007/s00285-014-0771-1>
9. Santos-Oliveira, P., et al.: The force at the tip-modelling tension and proliferation in sprouting angiogenesis. *PLoS Comput. Biol.* **11**, e1004436 (2015)
10. Mada, J., Matsuya, K., Yura, F., Kurihara, H., Tokihiro, T.: A mathematical modeling of angiogenesis. *JSIAM* **26**, 105–123 (2016)
11. Matsuya, K., Yura, F., Mada, J., Kurihara, H., Tokihiro, T.: A discrete mathematical model for angiogenesis. *SIAM J. Appl. Math.* **76**, 2243–2259 (2016)